NMR IN BIOMEDICINE
NMR Biomed. 2006; **19**: 188–197
Published online 13 January 2006 in Wiley InterScience (www.interscience.wiley.com). DOI:10.1002/nbm.1008

Quantification of prostate MRSI data by model-based time domain fitting and frequency domain analysis

Pieter Pels,[1,2]* Esin Ozturk-Isik,[2,3] Mark G. Swanson,[4] Leentje Vanhamme,[1] John Kurhanewicz,[4] Sarah J. Nelson[2,3] and Sabine Van Huffel[1]

[1]ESAT-SCD, Katholieke Universiteit Leuven, Leuven-Heverlee, Belgium
[2]Surbeck Laboratory of Advanced Imaging, Department of Radiology, University of California, San Francisco, CA 94158, USA
[3]UCSF/UCB Joint Graduate Group in Bioengineering, San Francisco, CA 94143, USA
[4]Department of Radiology, University of California, San Francisco, CA 94158, USA

Received 10 June 2005; Revised 9 September 2005; Accepted 18 October 2005

ABSTRACT: This paper compares two spectral processing methods for obtaining quantitative measures from *in vivo* prostate spectra, evaluates their effectiveness, and discusses the necessary modifications for accurate results. A frequency domain analysis (FDA) method based on peak integration was compared with a time domain fitting (TDF) method, a model-based nonlinear least squares fitting algorithm. The accuracy of both methods at estimating the choline + creatine + polyamines to citrate ratio (CCP:C) was tested using Monte Carlo simulations, empirical phantom MRSI data and *in vivo* MRSI data. The paper discusses the different approaches employed to achieve the quantification of the overlapping choline, creatine and polyamine resonances. Monte Carlo simulations showed induced biases on the estimated CCP:C ratios. Both methods were successful in identifying tumor tissue, provided that the CCP:C ratio was greater than a given (normal) threshold. Both methods predicted the same voxel condition in 94% of the *in vivo* voxels (68 out of 72). Both TDF and FDA methods had the ability to identify malignant voxels in an artifact-free case study using the estimated CCP:C ratio. Comparing the ratios estimated by the TDF and the FDA, the methods predicted the same spectrum type in 17 out of 18 voxels of the *in vivo* case study (94.4%). Copyright © 2006 John Wiley & Sons, Ltd.

KEYWORDS: MR spectroscopy; prostate cancer; quantification; time domain; frequency domain; citrate; choline; polyamines

INTRODUCTION

Prostate cancer is the most frequently diagnosed type of cancer and the second leading cause of cancer deaths among American men (1). Digital rectal examination, transrectal ultrasound (TRUS) guided sextant biopsy and prostate-specific antigen (PSA) screening are the three most widely used clinical tools for the diagnosis and staging of prostate cancer (2). Combined volumetric magnetic resonance imaging and three-dimensional MR spectroscopic imaging (MRI/3D-MRSI) is a rapidly growing non-invasive technique that provides both high-resolution anatomical images of the prostate and surrounding tissues and a quantitative assessment of prostate metabolism in a single one-hour exam. Combined MRI/3D-MRSI has been shown to improve the localization (3) and staging (4) of prostate cancer, provide a measure of prostate cancer aggressiveness (5) and tumor volume (6), and has been useful for planning treatment (7–10) and evaluating therapeutic response (11–15).

3D-MRSI provides arrays of individual prostate spectra that are characterized by three major metabolite peaks: the singlets choline and creatine and the strongly coupled citrate multiplet, which appears as an overlapping doublet of doublets at 1.5 T. Healthy glandular prostate tissue also demonstrates high levels of polyamines (predominantly spermine), which resonate between choline and creatine, but cannot be completely resolved. Within the peripheral zone, regions of prostate cancer demonstrate higher levels of total choline and reduced levels of citrate and polyamines compared with healthy peripheral zone tissues. The increase in choline-containing phospholipid metabolites in prostate cancer has been attributed to a number of factors including an increase in cellular proliferation and cell density, as well as alterations in signal transduction pathways during carcinogenesis (16,17). The decrease in citrate and polyamines in prostate cancer is due to changes in cellular function combined with the replacement of the tissue's characteristic ductal morphology (5,18).

**Correspondence to:* P. Pels, Surbeck Laboratory of Advanced Imaging, University of California, San Francisco, QB3 Building 3rd floor, Suite 303, 1700 4th Street, San Francisco, CA 94158, USA.
E-mail: pieter.pels@mrsc.ucsf.edu

Abbreviations used: BASING, band selective inversion with gradient dephasing; CCP:C, choline + creatine + polyamines to citrate ratio; FDA, frequency domain analysis; PSA, prostate-specific antigen; TDF, time domain fitting; TRUS, transrectal ultrasound.

Copyright © 2006 John Wiley & Sons, Ltd.

The development of mathematical routines for reconstructing and correcting 3D-MRSI data is important for quantifying the metabolic content of the tissue of interest. Two major strategies for extracting quantitative information from spectral data are time and frequency domain-based methods. In the time domain approaches, after a Fourier transform of *k*-space, the array of free-induction decay (FID) signals is typically analyzed on a voxel-by-voxel basis using a mathematical model that includes the concentration, resonance frequency, damping and phase parameters of the metabolites. Frequency domain processing methods apply both *k*-space and time domain Fourier transforms to provide a spatial array of spectra. Peak finding and fitting routines are then applied to estimate similar parameters for the metabolites of interest. Several studies have been conducted to compare different time and frequency domain-based approaches for accurate quantification of ^{13}C spectra from liver (19), ^{31}P spectra from rat tumors (20) and ^{1}H spectra from blood plasma (21), brain (22–24) and brain simulations (25).

The overlapping choline, creatine and polyamine peaks and the citrate multiplet observed in prostate ^{1}H spectra pose a new and unique challenge for time and frequency domain fitting methods. In this study we compared two spectral data processing approaches that have been used for clinical data processing: a time domain fitting (TDF) approach based on an Advanced Method for Accurate, Robust, and Efficient Spectral fitting ($AMARES_f$) (26,27), and an automated frequency domain analysis (FDA) procedure (28). These methods were evaluated in terms of the accuracy of parametric quantification of choline, creatine and citrate. Monte Carlo simulations, empirical data from phantoms and *in vivo* data from prostate cancer patients were used to assess the quantitative effectiveness of the two methodologies.

METHODS

Simulations

Spectra representing a phantom solution, healthy peripheral zone tissue, mixed tumor and healthy peripheral zone tissue, moderately aggressive and very aggressive tumors were simulated using a sum of K decaying exponentials as shown in equation (1),

$$y(n) = \sum_{k=1}^{K} a_k e^{j\phi_k} e^{(-d_k + j2\pi f_k)t(n)} \qquad n = 0, 1, \ldots, N-1 \tag{1}$$

where $y(n)$ is the nth point of the simulated signal. Parameters a_k, f_k, d_k and ϕ_k denote the amplitude, frequency, damping and phase of the kth resonance, respectively, and $t(n) = n\Delta t$ a time variable with Δt the sampling interval. The dampings and frequencies were selected based upon *in vivo* prostate data acquired at 1.5 T. The levels of choline, creatine, citrate and polyamine resonances corresponding to each of the five different spectral patterns are shown in Fig. 1. Citrate was modeled as two large center peaks and two small side peaks to mimic its spectral appearance at 1.5 T and $TE = 130$ ms. Choline, creatine and polyamines were modeled as single resonances. All peaks had a damping of 2 Hz except for polyamines, which had a damping of

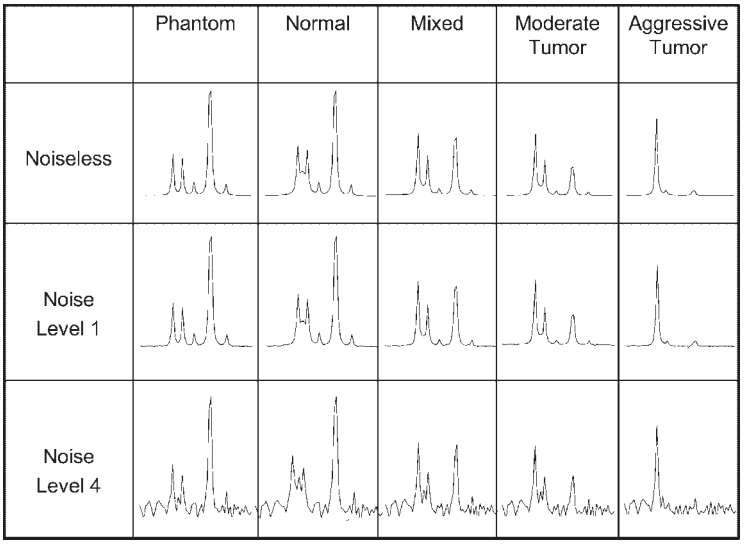


Figure 1. The five different spectral types used in the Monte Carlo simulations, each shown with no noise added (upper row), the lowest noise level added (middle row) and the highest noise level added (bottom row).

Copyright © 2006 John Wiley & Sons, Ltd.

8 Hz. The time and frequency domain analysis methods were applied to calculate the ratio of (choline + creatine + polyamines) to citrate (CCP:C).

The accuracy of the ratio estimates was compared for the simulations using the relative root mean square error (RMSE) and relative bias, which are defined as,

$$\text{Relative RMSE ratio} = 100\sqrt{\frac{1}{L}\sum_{l=1}^{L}\frac{(\text{ratio}_{\text{ex}} - \text{ratio}_l)^2}{\text{ratio}_{\text{ex}}^2}} \quad (2)$$

$$\text{Relative bias} = 100\frac{\text{ratio}_{\text{ex}} - \frac{1}{L}\sum_{l=1}^{L}\text{ratio}_l}{\text{ratio}_{\text{ex}}} \quad (3)$$

where ratio_{ex} is the exact ratio of CCP:C, ratio_l is the estimate of the ratio for simulated signal l and L is the total number of simulations.

Monte Carlo analysis was employed to evaluate the relative RMSE, relative bias and standard deviation of the CCP:C ratio estimate for each of the five model functions. Four levels of random white noise with Gaussian distributions were selected to produce signal-to-noise ratios (SNR) of 170, 35, 15.5 and 10 for the choline peak of the simulated normal spectrum. Signal-to-noise ratio was defined as the height of the choline peak divided by the standard deviation of the noise in the frequency domain. Figure 1 shows the original noiseless spectra for each of the five different cases, along with the spectra containing the minimum and maximum levels of noise. Two hundred realizations of each noise level were added to each of the five model functions.

Phantom and *in vivo* data acquisition

A phantom solution was prepared to approximate the normal concentrations of the major prostate metabolites choline (4 mM), creatine (30 mM) and citrate (132 mM), and was placed into a 560 ml plastic spherical container. Both phantom and *in vivo* MR studies were performed on a 1.5 T GE Signa clinical MR scanner (GE Medical Systems, Milwaukee, WI, USA) using the body coil for excitation and a combined endorectal/pelvic phased array coil system for signal reception (Medrad, Pittsburg, PA, USA). Informed consent was obtained from nine human subjects prior to undergoing MRI/3D-MRSI staging examinations.

The imaging protocol included a sagittal scout, followed by axial T_1-weighted spin echo images ($TR = 600$ ms, $TE = 12$ ms, 256×192 matrix) for human subjects, and axial T_2-weighted fast spin echo images (5000–6000/108 ms effective, 256×192 matrix) for both human and phantom studies. Spectroscopic data were acquired using PRESS volume localization with three-dimensional phase encoding on a $16 \times 8 \times 8$ matrix at a nominal spatial resolution of $0.34\,\text{cm}^3$, with TR:$TE = 1000$:130 ms, and total acquisition time of 17:08 min. For phantom studies, a $50 \times 30 \times 30$ mm PRESS volume was prescribed using the axial T_2 weighted images and placed as close as possible to the endorectal coil while avoiding the edges of the sphere. For *in vivo* spectroscopy, the PRESS volume selection was prescribed using the axial T_2 weighted images to encompass as much of the prostate as possible while excluding periprostatic lipids and the rectum. Water and lipid suppression were achieved using the band selective inversion with gradient dephasing (BASING) technique (29). Spatially selective saturation pulses were employed to eliminate signals from regions outside the phantom, periprostatic lipid contamination and susceptibility-induced artifacts caused by the air-tissue interface of the rectum (29).

Phantom and *in vivo* MRSI data reconstruction

The phantom and *in vivo* data were first processed using voxel shifting and three-dimensional Fourier transforms to generate arrays of spatially localized time domain signals centered upon the PRESS selected volume. These data were further processed with 2 Hz Gaussian time domain apodization, followed by Fourier transformation and automated phasing to generate three-dimensional arrays of spatially localized spectra that could be directly correlated with the anatomical images (28).

A total of 72 voxels from within the PRESS box were selected from the phantom data. The arrays of *in vivo* spectra were compared with the anatomical images and 72 voxels were identified from the peripheral zone and central gland that had good SNR and were free of lipid contamination. Signals corresponding to the selected phantom and *in vivo* voxels were extracted for the two analysis methods. A slice of data was selected from an *in vivo* MRSI dataset that contained biopsy-confirmed regions of tumor and normal tissue for cancer assessment.

Time domain processing

The MRSI data were transformed from k-space to the spatial domain, leaving the time direction unaffected. To achieve estimates of the amplitudes, frequencies, dampings and phases of the different resonances in the spectra, the signals were modeled in the time domain, with the model function as described in equation (1). The algorithm AMARES_{f} (26,27) was used to find the optimal estimates of the parameters of the original signal by minimizing the following cost function,

$$\sum_{n=1}^{N}\left|y(n) - \sum_{k=1}^{K}h^{\text{T}}b_k\left(a_k e^{j\phi_k}e^{(-d_k + j2\pi f_k)t(n)}\right)\right|^2 \quad (4)$$

A finite impulse response (FIR) filter was included in the minimization process to eliminate any residual water

Copyright © 2006 John Wiley & Sons, Ltd.

and lipid that could be present in the signals (27). The cost function included an automatically designed filter vector h and a vector b, containing signal components. Filter vector h was designed in such a way that product $h^T b_k$ was zero for certain k, thereby eliminating those resonances.

The algorithm allowed the inclusion of *a priori* knowledge on the parameters, which improved the accuracy of parameter estimation (26,27). For example, the frequency shift between the peaks of the inner doublet of citrate was known from quantum-mechanical calculations for the strongly coupled AB system of citrate (30). The AMARES$_f$ algorithm requires starting values for the estimates of the frequencies, dampings and overall phase. Starting values for the frequencies were chosen as follows. First, initial estimates of frequency starting values were assessed visually from a reference spectrum. Next, the initial estimates were corrected for frequency shifts using the position of the water resonance from the same spectrum, since the difference in frequency between water and the metabolites of interest remains fairly constant. The starting value of the overall phase was given by the angle of the first complex datapoint of each signal, and the starting value for the damping was always 2.13 Hz. The algorithm also allowed the definition of upper and lower limits on the estimated parameters. Besides natural constraints, such as the amplitudes and dampings being positive, the boundaries of the frequencies were chosen in between the starting values of the different peaks, so that a peak in the spectrum would not be fitted by a neighboring peak in the model.

Besides the prior knowledge, the number of components in the model function (or model order) had to be adjusted for each signal type. Ideally, the model order equals the number of components present in the signals, but in some cases the nature of the spectra required a reduction of model order to increase the robustness of quantification. The model function used to quantify the simulation signals modeled all the peaks present in the spectrum, including single peaks corresponding to choline, creatine, and polyamines and four peaks corresponding to citrate. The following constraints were imposed on the estimated parameters: (1) shifts between the estimated frequencies of the citrate multiplet were fixed such that the frequency difference between the outer peaks and the inner peaks was 15 Hz and the frequency difference between the inner doublet peaks was 2.54 Hz; (2) the amplitudes of the outer lobes of citrate were equal, as well as the amplitudes of the inner doublet peaks; and (3) dampings of all peaks except polyamines were set to be equal. A stopband FIR filter was applied to the signals prior to fitting in order to eliminate the effect of the residual water resonances.

The presence of polyamines in the model spectra caused a large error in the estimation of damping and amplitude for choline, creatine and citrate, due to their overlap with both choline and creatine, and the lack of *a priori* knowledge of the linewidth. This was confirmed by calculating the Cramer–Rao lower bounds (CRB) on the parameter estimates for a six- and seven-peak model. The CRB indicates the best possible accuracy of an estimate for any unbiased estimator (31). The CRB on the relative RMSE of the CCP:C ratio increased 11% (normal) or 81% (phantom) when polyamines were included in the model. Based on the results of the CRB analysis, the simulated signals were processed using a six-peak model, including choline, creatine and four citrate peaks. The choline and creatine were modeled more accurately using the six-peak model, leaving the polyamines behind in the residue. Only the first 256 points were used in the minimization problem. The same model function and filter were used to quantify the phantom data, because no polyamines were included in the phantom solution.

For *in vivo* processing, polyamines and the outer peaks of citrate were left out of the model function to increase the robustness of the quantification, leading to a four-peak model, including only choline, creatine and the inner citrate doublet peaks. Quantifying polyamines was difficult because they were highly overlapping with choline and creatine. Additionally, polyamines and the outer wings of citrate were very small for the *in vivo* case. A passband filter that coincided with the metabolite region was also chosen for filtering the *in vivo* data. The filter passband was 1.9 ppm wide and was positioned to eliminate the residual water and lipid resonances outside the metabolite region at the same time.

Frequency domain analysis

The FDA used in this study (28) was an automated procedure composed of routines for reconstruction and correction of the spectral data for frequency, phase and baseline distortions, and final estimation of the parameters for the peaks of interest. The analysis was initiated by apodizing the FIDs in the time domain with a Gaussian filter of 2 Hz, followed by fast Fourier transformation (FFT) from the time to the frequency domain. Data acquisition parameters were extracted from the header of the reference MR images for accurate registration of the spectra to the anatomical images and for correct interpretation. Discrete Fourier transformation (DFT) was applied to the data to generate a three-dimensional array of spectra on a rectangular grid based on the coordinate system of the reference anatomical images. The center of the grid was spatially shifted to reduce the partial volume effects around the edges of the excited region and to maximize the full tissue voxels.

Frequency shifts were corrected for each spectrum based on a peak descriptor file, which included the expected locations and linewidths of water, choline, creatine and citrate peaks. Separate peak descriptor files for the phantom and *in vivo* cases were established by

Copyright © 2006 John Wiley & Sons, Ltd.

inspecting several empirical phantom and human prostate spectra, respectively. The peak file that was used for the simulated data was generated to match the peak locations of the simulations. A statistical peak finding routine was applied to the magnitude data (28) to locate the frequencies of each peak of the spectrum. The frequency shift for each peak was estimated as the difference between the peak location found by the algorithm and the location given in the peak descriptor file. The mean of the frequency shifts of all the peaks was applied to the spectrum as the estimated frequency correction.

An automatic phase correction algorithm (28) was used to find the value that maximized the area of the real part, while minimizing the area of the imaginary part of the spectrum. Baseline removal routines assumed that the spectra were a sum of the peaks, baseline, residual water and random noise, and iteratively separated these components. The algorithm isolated the data points that corresponded to the spectral peak regions by using the locations and linewidths given in the peak descriptor file at the first iteration. Variations of the peak parameters for the given data were inspected, and used for further iterations.

After the baseline correction, peak locations and heights were determined by searching for a maximum in each of the peak regions. Peak areas were calculated by integrating over the peak regions given in the peak descriptor file in the real part of the spectrum. Choline, creatine and polyamines were not resolvable due to spectral overlap, and their area sum was calculated by integrating over their combined region.

RESULTS

Simulations

Relative RMSE and bias calculations were used to compare the accuracy of time and frequency domain methods for the CCP:C ratio estimations of the simulated signals. The FDA method was unable to estimate separate levels of choline, creatine and polyamines due to the overlap of these three peaks, whereas the TDF method required the exclusion of polyamines to reduce the error as described in the Methods section. The relative RMSE and biases for the five different simulation signals are presented in Table 1. It should be noted that the standard deviation did not increase linearly over the four different noise levels. Both FDA and TDF methods resulted in stable ratio estimates for the mixed, normal, phantom and tumor cases. The maximum relative RMSE increase was 7.79% for TDF, and 12.35% for FDA as the SNR decreased for these four cases. Very low levels of citrate were present in the aggressive tumor spectrum simulation, leading to almost zero estimates for citrate and forcing the ratios to extremely large numbers. Ratios were withheld if their absolute values were larger than 150 to prevent the distortion of the RMSE and bias calculations. The TDF algorithm did not converge for a few voxels, resulting in zero amplitude estimates for all of the peaks, and undefined ratio. Those results were also excluded from the analysis. The exclusion of results was only necessary in the aggressive tumor case, and 0, 7, 7 and 15 results out of each of the 200 iterations were withheld from the statistical analysis for the four different noise levels respectively. Table 1 shows that the TDF method was more accurate in four of the five simulated signals, specifically, the aggressive tumor, mixed (tumor and normal), phantom and moderately aggressive tumor cases.

The influence of fast T_2 decaying resonances such as polyamines was lowered by deleting the first data points of the time domain signal, beyond which they are largely damped out. It was found that deleting nine points resulted in the most accurate estimate of the CCP:C ratio. The number of points that results in the minimum error is determined by balancing two counteracting mechanisms, the reduction of the bias due to decreasing the influence of polyamines, and the increase in the relative standard deviation due to dismissing the points with the most energy. The relative RMSE of the TDF method for the normal spectrum decreased to 17.7, 18.7, 18.8 and

Table 1. Relative RMSE and relative bias of Monte Carlo simulations

		Relative RMSE (%)				Relative bias (%)			
		Noise 1	Noise 2	Noise 3	Noise 4	Noise 1	Noise 2	Noise 3	Noise 4
Aggressive tumor	TDF	7.66	25.14	54.29	303.69	6.32	10.33	14.49	2.46
	FDA	44.79	250.27	282.50	225.29	−39.80	−52.37	41.22	79.34
Mixed	TDF	8.77	9.30	10.69	12.53	8.75	8.96	9.19	9.39
	FDA	12.15	12.88	13.99	16.33	12.14	12.49	12.15	12.28
Normal	TDF	26.58	26.75	27.06	27.43	26.58	26.71	26.86	26.96
	FDA	18.31	18.40	21.56	24.22	18.31	18.32	21.07	23.43
Phantom	TDF	0.50	2.45	5.38	8.29	0.11	0.26	0.37	0.33
	FDA	9.07	9.59	11.30	13.66	9.05	9.14	9.34	9.42
Moderate tumor	TDF	8.90	10.01	12.90	16.67	8.87	9.13	9.34	9.65
	FDA	11.49	13.05	16.61	23.84	11.43	11.77	10.10	8.79

Copyright © 2006 John Wiley & Sons, Ltd.

20.4% for the four different noise levels, respectively, when nine initial data points were deleted, resulting in more accurate estimates at the first, third, and fourth noise levels than the FDA method.

Phantom

The first three plots of Fig. 2(a) show the choline, creatine and citrate estimates by TDF method vs the FDA method. The Spearman rank correlation coefficients were calculated to determine the association between the amplitude and area estimates of the time domain fitting and frequency domain analysis methods. The Spearman rank correlation coefficients were 0.99 for choline, 0.89 for creatine and 0.97 for citrate estimates ($p < 0.05$ for all three metabolites). The results of the two methods were in good agreement both visually and statistically. A cloud of points with center $(0.59 \pm 0.074,\ 0.55 \pm 0.049)$ that corresponded to the means of the TDF and FDA estimates was observed. The distribution of the estimates for the different voxels is illustrated in Fig. 3. In three voxels the time domain fitting failed to include the creatine peak, resulting in a lower estimate of the ratio (voxels 41–43). Two other outliers were due to a phase artifact present in the citrate doublet, leading to an incorrect estimate for the citrate resonance by the TDF method.

In vivo data

The estimates of the areas and amplitudes of the different metabolites were more difficult to evaluate for *in vivo* voxels due to the lower signal-to-noise ratio of the data.

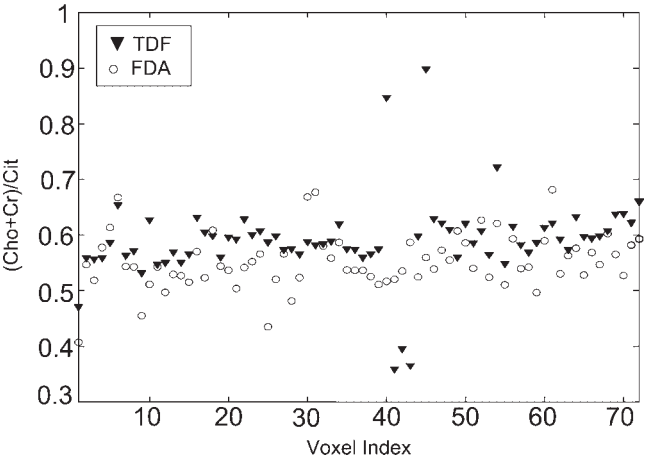


Figure 3. CC:C ratio estimates of the two methods for 72 phantom voxels.

This was reflected as an increase in the difference of the estimates that were calculated by the two methods, as shown in Fig. 2(b). The Spearman rank correlation coefficients were smaller for the *in vivo* metabolite estimates than for the phantom case, specifically, 0.59 for choline, 0.51 for creatine, 0.94 for citrate, and the coefficient for the ratio was 0.8. All of the correlations were significant with $p < 0.05$. Figure 4 shows the estimated ratios for all of the selected *in vivo* voxels. The time domain fitting failed to converge to a solution in one voxel, yielding zero estimates for all amplitudes.

Based upon 3D-MRSI data acquired from thousands of patients, various CC:C thresholds have been used clinically to distinguish normal, probable tumor and definite tumor. Such CC:C thresholds are arbitrary and can be changed to meet different clinical demands of sensitivity

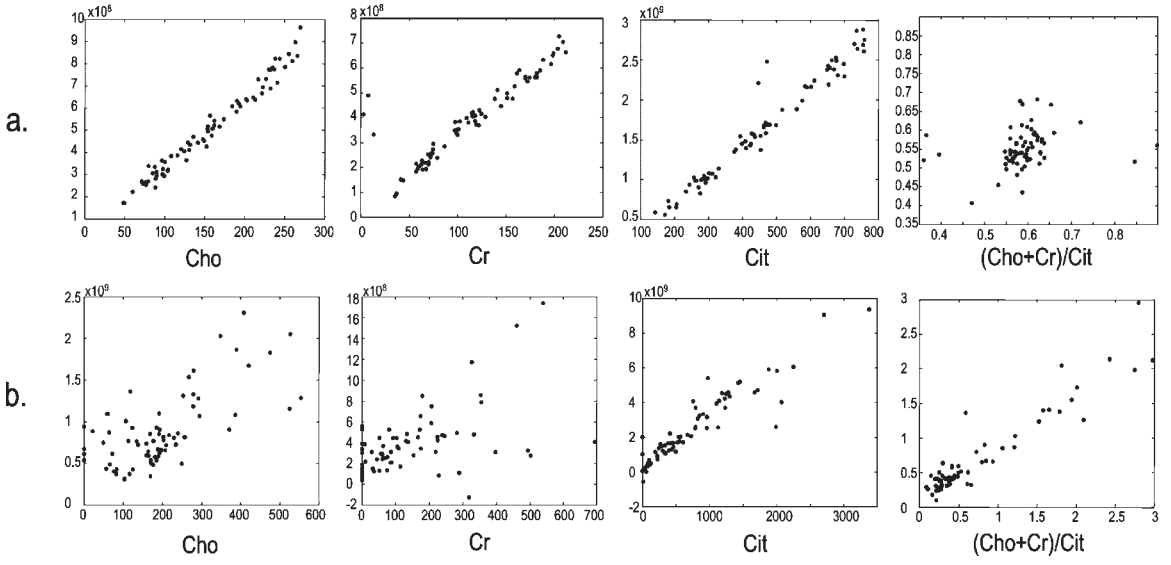


Figure 2. (a) Scatter plots of choline, creatine, citrate, and CC:C ratio calculated from TDF vs FDA methods for 72 phantom voxels. (b) Scatter plots of choline, creatine, citrate and CCP:C ratio calculated from TDF vs FDA methods for 72 *in vivo* voxels.

Copyright © 2006 John Wiley & Sons, Ltd.

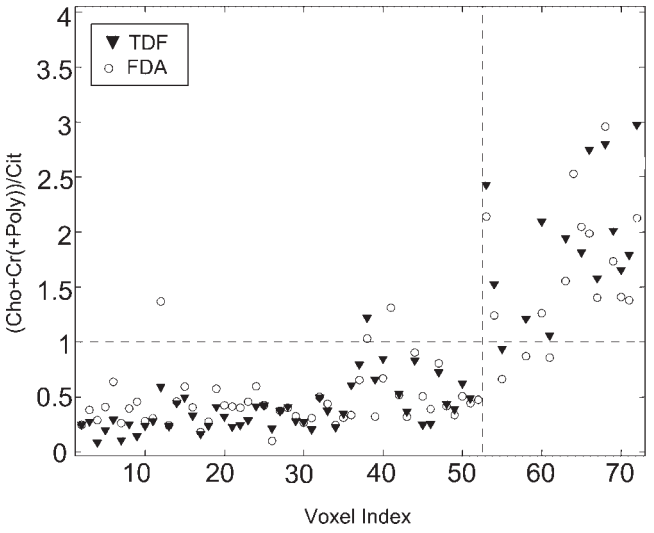


Figure 4. CCP:C ratio estimates of the two methods for 72 *in vivo* voxels. The horizontal line indicates CCP:C = 1, which was chosen as the threshold to discriminate between the healthy and tumor spectra. The vertical line divides the voxels coming from a tumor region and those from healthy voxels.

and specificity. Typically, a CC:C ratio < 0.5 indicates normal healthy metabolism, a CC:C ratio between 0.5 and 0.86 indicates possible or probable cancer, and a CC:C ratio > 0.86 indicates cancer. For the current analysis, a threshold CC:C ratio of 1 (horizontal dashed line on Fig. 4) was chosen to select only voxels in the clear-cut cancer range. Both time and frequency domain methods predicted the same voxel condition for 94% of the voxels (68 out of 72). The TDF method estimated the damping (or linewidth in the frequency domain) of each of the peaks, which indicated the quality of the shimming. The mean value of the dampings was 18.8Hz with a standard deviation of 9.3 Hz.

Case study

Figure 5 illustrates frequency domain versus time domain fitting using a two-dimensional spectral array (slice) from a 3D-MRSI exam. The T_2 weighted image (a) and corresponding spectral array (b) show a region of mixed cancer and normal peripheral zone tissue on the right side of the gland (left side of image/array), and a region of very aggressive cancer on the left side of the gland (right side of image/array). The results of the time domain fitting for all voxels in one slice of an *in vivo* study are shown in Fig. 5(d). The residual signals, which are shown in Fig. 5(c), are the difference between the original signals and the model signals fitted by the TDF method without any line broadening filter. The spectra shown in Fig. 5(b) were obtained after the preprocessing FDA steps described in the Methods section, and were also used for the area integration part of the frequency domain analysis.

DISCUSSION

The RMSE of the estimation of the CCP:C ratio for the simulated prostate spectra was mainly due to the bias error in both methods as is shown in Table 1. Both

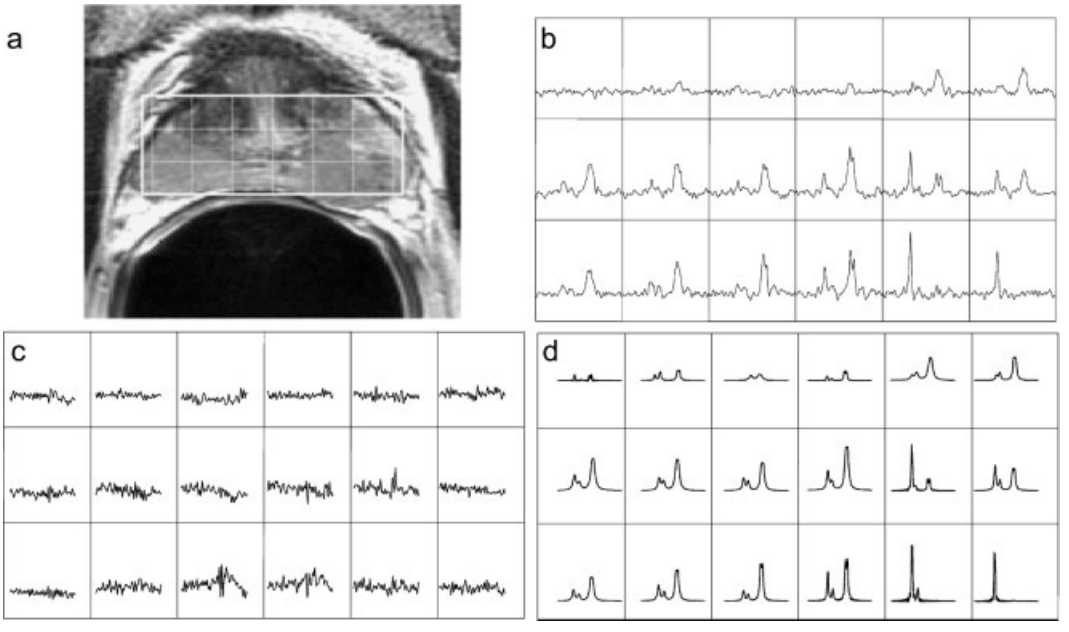


Figure 5. (a) Axial T_2 weighted image of the prostate with superimposed position of the voxels within the PRESS box. (b) Spectra from within the PRESS box after FDA method's preprocessing. (c) Residual difference between the original spectra (not shown) and the estimated spectra in (d). (d) Estimated fits of the spectra produced by the TDF method.

Copyright © 2006 John Wiley & Sons, Ltd.

methods underestimated the ratio but for different reasons. Underestimation was caused by leaving the polyamines out of the ratio calculation for the TDF method. The error increased with the amplitude of the polyamines, as indicated by the higher relative RMSE error of the TDF method in tumor or mixed signals compared with the phantom signal, which did not contain polyamines. Even when the polyamines were omitted, the TDF method provided more accurate ratio estimates than the FDA method in all cases except for the normal simulation signal. Underestimation of the ratio by the FDA method can be explained as follows. The FDA method integrated pre-defined areas under the peaks, which might have excluded some of the peak tails. The baseline removal algorithm may also have marked parts of the peak tails as a part of the baseline and reduced their amplitude.

As can be seen in Table 1, the RMSE of the ratio estimate increased tremendously (from 54.29 to 303.69%) from the third to the fourth noise level for the case of the aggressive tumor simulations. This can be explained by the fact that the CCP:C ratio of the aggressive tumor simulation signals is very sensitive to the citrate estimate because the citrate amplitude is very small (almost zero). It is clear that, owing to these high RMSE values, the estimate of the bias is less meaningful than for small RMSE values but is more dependent on the outliers in the CC:C estimates. This explains the drop in bias for the fourth noise level.

The negative influence of polyamines can be reduced by deleting the initial data points in the TDF quantification process. However, this method is only useful when applied to spectra that contain polyamines; otherwise, the relative RMSE would increase due to the reduction of the overall SNR. The bias and RMSE were relatively high in the aggressive tumor simulations owing to the low citrate values in the denominator of the estimated parameter, but were not representative of the method's ability to differentiate tumor spectra. While this would have been of concern if the objective had been to get a precise estimate of the CCP:C ratio, both methods were successful in identifying tumor tissue, provided that the CCP:C ratio was greater than a given (normal) threshold.

The analysis and quantification were more complicated for the phantom data compared with the simulations. Simulated signals were ideal, with all Lorentzian peaks and Gaussian noise. Acquisition artifacts, such as the lineshape or phase distortions and relaxation time effects, were also absent in the simulated data. The variance of the estimates for TDF and FDA methods were 0.074 and 0.049, respectively, which were high due to the acquisition related errors.

The *in vivo* data showed lower correlation coefficients for the estimates of the metabolites, while the correlation coefficient for the ratio was larger for the *in vivo* than the phantom case. This was due to the fact that there was a larger range of ratios present in the *in vivo* dataset. The type of tissue within the voxel was clearly reflected in the ratios calculated by both methods. A higher ratio was estimated for 20 voxels containing tumor, which are located on the right side of the vertical dashed line in Fig. 4.

A visual interpretation of the fits of the TDF method in the case study showed that they represented the original signals well. Some of the residues showed parts of peaks that were not accounted for in the modeled fit. This was due to the modeling errors, coming from the deviations in the spectra from the model function. As described in the previous paragraph, the ratios can be used for discriminating healthy from tumor spectra. Comparing the ratios predicted by the TDF and the FDA, the methods predicted the same spectrum type in 17 out of the 18 voxels (94.4%). Only the voxel in the top left corner was predicted 'healthy' by the TDF method and 'tumor' in the FDA method, and it was difficult to predict the condition of this voxel due to the low signal-to-noise ratio in that particular voxel.

Simulations showed that the TDF method was able to make more accurate estimates than the FDA method for the ratio when spectral peaks were well resolved and the contribution of the underlying polyamines was relatively small. In this case, the TDF method was able to give individual estimates for different peaks of choline, polyamines and creatine, where the FDA method was only able to estimate the sum of the areas under the three peaks. The TDF method was, however, sensitive to distortions in the lineshape of the resonances and other acquisition induced distortions, which can cause errors on estimates as well as non-convergence of the algorithm. The FDA method is less sensitive to data acquisition problems, and will result in a robust estimate for almost any types of spectrum. Both methods were able to deal with frequency shifts, but handled them differently. For the TDF method, starting values were supplied, which were corrected for frequency shifts using the position of the water peak. After that, the algorithm automatically searched for the optimal position of the peaks, taking *a priori* knowledge into account. The FDA method also used a frequency alignment procedure based on the position of the water resonance, but in some cases manual correction of the peak locations was applied to achieve more accurate area estimates, because frequency shifts affected the estimates due to the integration of predefined areas. Although both methods estimated the phases automatically, further manual phase corrections were sometimes needed in the FDA based upon manual inspection of the data.

CONCLUSIONS

Previous studies (19–25) reported comparisons of various time and frequency domain-based spectral processing methods, but to our knowledge there has not been a comprehensive study of the effectiveness of processing methodologies for prostate ^{1}H spectra. This study

Copyright © 2006 John Wiley & Sons, Ltd.

compared two data processing approaches, time domain-based TDF and frequency domain-based FDA, for the performance of their spectral parameter estimates on prostate ^{1}H spectra from simulations and empirical phantom and patient data. While the FDA method was not able to resolve the overlapping choline, creatine and polyamine resonances and the TDF method had to omit the polyamines from the model function to obtain parameter estimates, both TDF and FDA methods still had the ability to identify cancerous voxels for an artifact-free case study using the ratio of choline + creatine + (polyamines) to citrate. This is suggested as an effective and robust metric for prostate spectral assessment at 1.5 T. Spectral overlap in prostate data acquired at 1.5 T was a factor reducing the accuracy of quantification for both of the processing techniques. The TDF method had some problems in modeling the spectra with low SNR. Preliminary results from 3 T scanners exhibit higher SNR, and improved spectral resolution with visually separable polyamines. This will probably increase the accuracy of quantification for both methods in the future.

The most appropriate choice of the data processing method for any specific application depends on the purpose of the quantification and the type of the spectra analyzed. The results of this study support the use of the TDF method for accurate quantification of the spectra with good SNR, and its ability to separate sharp resonances from the broader peaks. The FDA method is valuable for robust and fast quantification of the spectra, even when there are acquisition-related distortions in the spectra. Both of these processing methodologies are suitable for routine analysis of prostate spectra for clinical and research purposes.

Acknowledgements

The authors would like to thank Mr Daniel Lee and Mr Chris Sotto, University of California, San Francisco, for their help with data preparation. P.P. was supported by an IWT grant of the Flemish Institute for the Promotion of Scientific-Technological Research in Industry. L.V. was supported by the National Fund for Scientific Research FWO-Flanders. S.V.H. is supported by the framework of the Belgian Program on Interuniversity Poles of Attraction, initiated by the Belgian State, Prime Minister's Office of Science, Technology and Culture (IUAP P5-22), the Concerted Action Project AMBioRICS of the Flemish Community, the FWO projects G.0407.02, G.0078.01, G.0269.02, G.0270.02, EU integrated project ETUMOUR (contract no. FP6-2002-LIFESCIHEALTH 503094) and EU Network of Excellence BIOPATTERN (contract no. FP6-2002-IST 508803). This study was also supported by a University of California Discovery Grant (LSIT-01-10107), General Electric Medical Systems, and grants from the National Cancer Institute, NIH (R01 CA59897 and K01 CA96618).

REFERENCES

1. The American Cancer Society. *Cancer Facts and Figures*, 2004.
2. Dhingsa R, Qayyum A, Coakley FV, Lu Y, Jones KD, Swanson MG, Carroll PR, Hricak H, Kurhanewicz J. Prostate cancer localization with endorectal MR imaging and MR spectroscopic imaging: effect of clinical data on reader accuracy. *Radiology* 2004; **230**(1): 215–220.
3. Scheidler J, Hricak H, Vigneron DB, Yu KK, Sokolov DL, Huang LR, Zaloudek CJ, Nelson SJ, Carroll PR, Kurhanewicz J. Prostate cancer: localization with three-dimensional proton MR spectroscopic imaging—clinicopathologic study. *Radiology* 1999; **213**(2): 473–480.
4. Yu KK, Scheidler J, Hricak H, Vigneron DB, Zaloudek CJ, Males RG, Nelson SJ, Carroll PR, Kurhanewicz J. Prostate cancer: prediction of extracapsular extension with endorectal MR imaging and three-dimensional proton MR spectroscopic imaging. *Radiology* 1999; **213**(2): 481–488.
5. Kurhanewicz J, Swanson MG, Nelson SJ, Vigneron DB. Combined magnetic resonance imaging and spectroscopic imaging approach to molecular imaging of prostate cancer. *J. Magn. Reson. Imag.* 2002; **16**(4): 451–463.
6. Coakley FV, Kurhanewicz J, Lu Y, Jones KD, Swanson MG, Chang SD, Carroll PR, Hricak H. Prostate cancer tumor volume: measurement with endorectal MR and MR spectroscopic imaging. *Radiology* 2002; **223**(1): 91–97.
7. Kurhanewicz J, Swanson MG, Wood PJ, Vigneron DB. Magnetic resonance imaging and spectroscopic imaging: improved patient selection and potential for metabolic intermediate endpoints in prostate cancer chemoprevention trials. *Urology* 2001; **57**(4, suppl. A): 124–128.
8. DiBiase SJ, Hosseinzadeh K, Gullapalli RP, Jacobs SC, Naslund MJ, Sklar GN, Alexander RB, Yu C. Magnetic resonance spectroscopic imaging-guided brachytherapy for localized prostate cancer. *Int. J. Radiat. Oncol. Biol. Phys*. 2002; **52**(2): 429–438.
9. Zaider M, Zelefsky MJ, Lee EK, Zakian KL, Amols HI, Dyke J, Cohen G, Hu Y, Endi AK, Chui C, Koutcher JA. Treatment planning for prostate implants using magnetic-resonance spectroscopy imaging. *Int. J. Radiat. Oncol. Biol. Phys*. 2000; **47**(4): 1085–1096.
10. Zelefsky MJ, Cohen G, Zakian KL, Dyke J, Koutcher JA, Hricak H, Schwartz L, Zaider M. Intraoperative conformal optimization for transperineal prostate implantation using magnetic resonance spectroscopic imaging. *Cancer J*. 2000; **6**(4): 249–255.
11. Parivar F, Hricak H, Shinohara K, Kurhanewicz J, Vigneron DB, Nelson SJ, Carroll PR. Detection of locally recurrent prostate cancer after cryosurgery—evaluation by transrectal ultrasound, magnetic resonance imaging, and three-dimensional proton magnetic resonance spectroscopy. *Urology* 1996; **48**(4): 594–599.
12. Mueller-Lisse UG, Swanson MG, Vigneron DB, Hricak H, Bessette A, Males RG, Wood PJ, Noworolski S, Nelson SJ, Barken I, Carroll PR, Kurhanewicz J. Time-dependent effects of hormone-deprivation therapy on prostate metabolism as detected by combined magnetic resonance imaging and 3D magnetic resonance spectroscopic imaging. *Magn. Reson. Med.* 2001; **46**(1): 49–57.
13. Mueller-Lisse UG, Vigneron DB, Hricak H, Swanson MG, Carroll PR, Bessette A, Scheidler J, Srivastava A, Males RG, Cha I, Kurhanewicz J. Localized prostate cancer: effect of hormone deprivation therapy measured by using combined three-dimensional ^{1}H MR spectroscopy and MR imaging: clinicopathologic case-controlled study. *Radiology* 2001; **221**(2): 380–390.
14. Pickett B, Kurhanewicz J, Fein B, Coakley F, Shinohara K, Roach M. Use of magnetic resonance imaging and spectroscopy in the evaluation of external beam radiation therapy for prostate cancer. *Int. J. Radiat. Oncol. Biol. Phys*. 2003; **57**(2 suppl.): S163–S164.
15. Coakley FV, Teh HS, Qayyum A, Swanson MG, Lu Y, Roach M, Pickett B, Shinohara K, Vigneron DB, Kurhanewicz J. Endorectal

Copyright © 2006 John Wiley & Sons, Ltd.

MR and MR spectroscopic imaging of locally recurrent prostate cancer after external beam radiation therapy: preliminary experience. *Radiology* 2004; **233**(2): 441–448.
16. Ackerstaff E, Pflug BR, Nelson JB, Bhujwalla ZM. Detection of increased choline compounds with proton nuclear magnetic resonance spectroscopy subsequent to malignant transformation of human prostatic epithelial cells. *Cancer Res.* 2001; **61**: 3599–3603.
17. Kurhanewicz J, Swanson MG, Nelson SJ, Vigneron DB. Combined magnetic resonance imaging and spectroscopic imaging approach to molecular imaging of prostate cancer. *J. Magn. Reson. Imag.* 2002; **16**: 451–463.
18. Costello LC, Franklin RB, Narayan P. Citrate in the diagnosis of prostate cancer. *Prostate* 1999; **38**(3): 237–245.
19. Overloop K, Van Hecke P, Vanstapel F, Chen H, Van Huffel S, Knijn A, van Ormondt D. Evaluation of signal processing methods for the quantification of a multi-exponential signal: the glycogen ^{13}C-1 NMR signal. *NMR Biomed.* 1996; **9**(7): 315–321.
20. van den Boogaart A, Howe FA, Rodrigues LM, Stubbs M, Griffiths JR. *In vivo* ^{31}P MRS: absolute concentrations, signal-to-noise and prior knowledge. *NMR Biomed.* 1995; **8**(2): 87–93.
21. van den Boogaart A, Ala-Korpela M, Jokisaari J, Griffiths JR. Time and frequency domain analysis of NMR data compared: an application to 1D ^{1}H spectra of lipoproteins. *Magn. Reson. Med.* 1994; **31**(4): 347–358.
22. Kanowski M, Kaufmann J, Braun J, Bernarding J, Tempelmann C. Quantitation of simulated short echo time ^{1}H human brain spectra by LCModel and AMARES. *Magn. Reson. Med.* 2004; **51**(5): 904–912.
23. Elster C, Link A, Schubert F, Seifert F, Walzel M, Rinneberg H. Quantitative MRS: comparison of time domain and time domain frequency domain methods using a novel test procedure. *Magn. Reson. Imag*. 2000; **18**(5): 597–606.
24. Mullins PG, Rowland L, Bustillo J, Bedrick EJ, Lauriello J, Brooks WM. Reproducibility of ^{1}H-MRS measurements in schizophrenic patients. *Magn. Reson. Med.* 2003; **50**(4): 704–707.
25. De Beer R, Van den Boogaart A, Cady E, Graveron-Demilly D, Knijn A, Langenberger KW, Lindon JC, Ohlhoff A, Serrai H, Wylezinska-Arridge M. Absolute metabolite quantification by *in vivo* NMR spectroscopy: V. Multicentre quantitative data analysis trial on the overlapping background problem. *Magn. Reson. Imag.* 1998; **16**(9): 1127–1137.
26. Vanhamme L, van den Boogaart A, Van Huffel S. Improved method for accurate and efficient quantification of MRS data with use of prior knowledge. *J. Magn. Reson.* 1997; **129**(1): 35–43.
27. Sundin T, Vanhamme L, Van Hecke P, Dologlou I, Van Huffel S. Accurate quantification of ^{1}H spectra: from finite impulse response filter design for solvent suppression to parameter estimation. *J. Magn. Reson.* 1999; **139**(2): 189–204.
28. Nelson SJ. Analysis of volume MRI and MR spectroscopic imaging data for the evaluation of patients with brain tumors. *Magn. Reson. Med.* 2001; **46**(2): 228–239.
29. Star-Lack J, Nelson SJ, Kurhanewicz J, Huang LR, Vigneron DB. Improved water and lipid suppression for 3D PRESS CSI using RF band selective inversion with gradient dephasing (BASING). *Magn. Reson. Med*. 1997; **38**(2): 311–321.
30. Mulkern RV, Bowers JL. Calculating spectral modulations of AB systems during PRESS acquisitions. *Magn. Reson. Med*. 1993; **30**(4): 518.
31. Söderström T, Stoica P. *System Identification*. Prentice-Hall: London, 1998.

Copyright © 2006 John Wiley & Sons, Ltd.